Uncertainty Quantification of Guided Waves Propagation for Active Sensing Structural Health Monitoring

Shabbir Ahmed
PhD Student
Center for Mobility with Vertical Lift (MOVE)
Rensselaer Polytechnic Institute, Troy, NY, USA

Fotis Kopsaftopoulos
Assistant Professor
Center for Mobility with Vertical Lift (MOVE)
Rensselaer Polytechnic Institute, Troy, NY, USA

ABSTRACT

Guided-wave-based acousto-ultrasound structural health monitoring (SHM) methods have attracted the interest of the SHM community as guided waves can travel long distances without significant dissipation and are capable of detecting small damage sizes of several types. However, when subject to changing environmental and operational conditions (EOC), guided-wave-based methods may give false indications of damage as they exhibit increased sensitivity to varying EOC. In order to improve the reliability and enable the large-scale applicability of these methods, and to build a robust SHM system, it is necessary to quantify the uncertainty in guided wave propagation due to changing EOC. In this paper, a rigorous investigation on the uncertainty involved in the propagation of Lamb waves due to the variation in temperature and material properties of nominally-identical structures has been performed both numerically and experimentally. A high fidelity finite element model is established to study the effect of small temperature perturbation on the S_0 and A_0 modes of Lamb waves and the associated uncertainty is quantified. Then experiments are performed under ambient laboratory temperature variations during an eleven day period. The experimental results have indicated that temperature variations as small as 0.5 ^{0}C may result variations in the amplitude of Lamb waves and affect the damage index. Then uncertainty due to the variation in material properties has been considered by taking into account the statistical Gamma distributed dependency between Young's modulus and Poisson ratio jointly and the associated variation in the damage index is also investigated.

INTRODUCTION

In order to increase the reliability, safety and performance of aircraft/rotorcraft systems, it is pervasive to integrate Structural Health Monitoring (SHM) technologies (Ref. 1) which also enable the efficient life-cycle management of the system. SHM methods utilize distributed, permanently installed sensors at certain structural regions and apply diagnostic algorithms to extract meaningful health information from the sensing data. Such sensing data are subjected to various sources of uncertainty associated with all aspects of the inspection environment and operating conditions. In contrast to traditional nondestructive evaluation (NDE) procedures, where the factors due to operator pose the dominant uncertainty, SHM-based technologies are mainly challenged by in situ effects (Refs. 2–4). The robustness and accuracy of existing state-of-the-art SHM methods is questionable when exposed to different environmental conditions, such as temperature and humidity variations, as well as different loading and boundary conditions. The effect of varying environmental and operating conditions is to alter the sensing signals, oftentimes masking the effects of structural damage, and/or leading to false alarms and missed damage detection. When it comes to active-sensing acousto-ultrasound SHM techniques, a certain amount of uncertainty is inherent to the propagation of guided waves due to the varying environmental conditions and therefore, it is critical to quantify this uncertainty and properly take it into consideration in order to develop a robust SHM system, and enable proper reliability quantification and probabilistic decision making (Ref. 2).

Uncertainty quantification and propagation has become a subject of central importance as real world structures involve uncertainties due to material property variation, different manufacturing processes and varying environmental conditions. Engineering uncertainties are categorized into two broad classes, namely aleatory and epistemic uncertainties according to the nature of uncertainty sources (Ref. 5). Aleatory uncertainty stems from sources that are inherently random, such as the pressure field in a fully developed turbulent boundary layer. Epistemic uncertainty results from the incomplete or lack of knowledge, ignorance and modeling of a real physical system. In this paper, the case of epistemic uncertainty of guided wave propagation is considered.

Lamb waves are a type of guided waves that propagate through thin structures (Ref. 6). For performing active-sensing SHM based on lamb waves, a baseline or reference signal, usually from a healthy structure is subtracted from

---

Presented at the Vertical Flight Society 75th Annual Forum & Technology Display, Philadelphia, Pennsylvania, May 13–16, 2019.

later measurements, which yields a residual or scatter signal. Depending on the nature of this scatter signal, damage can be detected (see Figures 1 and 2). This method is known as Baseline Subtraction method. Recent studies have shown that by analyzing both numerically and experimentally the A_0 mode of Lamb wave propagation even a slight temperature change produces a level of residual or scatter signal that may mask the actual damage information, and thereby providing false indication of damage (Refs. 7–10). Temperature causes geometrical changes in a structure due to the increased molecular vibration of the materials which in turn causes changes in Young's modulus (Ref. 11). Temperature may also affect the boundary conditions of a system (Ref. 12). Again, the propagation velocity of both shear and longitudinal waves is dependent on Young's modulus. As a result, temperature changes the propagation velocities of these two waves, which imparts uncertainties in the propagation of Lamb waves.

In a recent study (Ref. 13), the authors have proposed a novel physics-based temperature compensation strategy. In this paper different physical properties, such as Young modulus, density, etc. of the base substrate, piezo-transducer, and adhesive interface were considered as functions of temperature and a functional relationship between the propagation of guided waves and temperatures were established. It was found that up to a certain temperature range this functional relationship is linear. Capitalizing on this information, a numerical temperature compensation model was proposed to relate the changes in the signal projection coefficients to the changes in the material properties induced by temperature variation. In order to verify this numerical scheme, experimental measurements were performed on flat rectangular aluminum plates and stiffened aluminum plates. Croxford et al. (Ref. 14) proposed a temperature compensation model where they used a combination of optimal baseline selection (OBS) and baseline signal stretch (BSS) methods. In the OBS method, multiple baseline measurements are required while in BSS method only a single baseline measurement is needed. In general, a temperature shift may alter the propagation of guided waves in such a way that it changes the shape, amplitude and arrival time of each of the individual wave packets. However, the change in the time of arrival may be considered as the dominant effect of changing temperature. In the OBS method, a best match is sought between the ensemble of collected baseline signal and the current signal. In BSS method, a stretch factor is used on the single baseline measurement to match the current signal.

In general, flaws exist in materials in the form of voids, defects and inclusions. Again, defects and in-homogeneity can be introduced in the materials by manufacturing processes. On the other hand, micro-structures are inherently stochastic in nature. Specimens made from the same manufacturing process may have point to point variations in the micro-structure as well as different specimens obtained from the same metal billet. This micro-structure variation may occur due to the stress and temperature gradient variability during processing. A varying degree of recrystallization after annealing may also contribute to the stochastic nature of micro-structures.

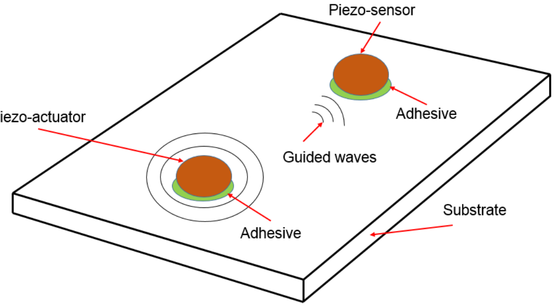

Fig. 1. Schematic diagram of the working principle of the acousto-ultrasound based SHM.

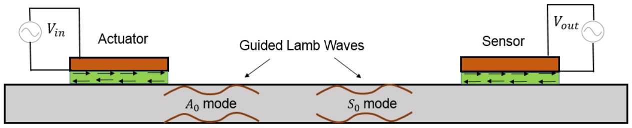

Fig. 2. Detailed side view of the substrate, adhesive and piezo sensors. Two modes of Lamb wave propagation, the symmetric (S_0) and antisymmetric (A_0), can be observed.

Therefore, it is natural that material properties such as Young's modulus, Poisson ratio and density may be also considered as random variables and can vary from specimen to specimen. If wave propagation in real structures is modeled assuming all material properties are a constant quantity, then a slight change in material properties from specimen to specimen or different parts of a large structure may give a false indication of damage. Because wave propagation in real structures can be altered due to such variations in material properties, corresponding damage indices are subsequently affected. As a result, in order to quantify the effects of variation in temperature and material properties and devise robust SHM methods that avoid false alarms of damage, it is essential to quantify the uncertainty involved in the process and observe and model the way damage indices are affected.

PROBLEM STATEMENT

It is a well known fact that Lamb waves are sensitive to different environmental and boundary effects such as temperature, humidity and loading conditions (Ref. 15). Although it is possible to acquire sufficient amount of baseline signals for data-driven environmental compensation models in a controlled or lab environment, it is not possible to capture baseline signals of all of the uncertain sources that a structure may be exposed to in service or its course of operation. In addition, it is not feasible in terms of the amount of time needed and cost involved. In this respect, a probabilistic model or approach for SHM systems in general, and environmental compensation in particular may go a long way. In this approach, only one baseline signal will be collected and a confidence interval will be provided based on the possible standard deviation of different uncertain sources.

However, in order to build this probabilistic model, it is required to have a deeper understanding of different uncertain sources and their associated uncertainties. Hence, the main objective of this paper is to rigorously investigate the uncertainty involved in Lamb wave propagation due to:

1. **Temperature variation:** How temperature imparts uncertainty in different modes of wave propagation by implementing numerical simulation and experimental investigation.
2. **Variation in material properties:** How different modes of wave propagation are affected by uncertainty in material properties from sample to sample or different structural elements of nominally-identical populations made of the same materials.

METHOD OF APPROACH

In order to address the uncertainty in the propagation of acousto-ultrasound diagnostic waves in isotropic materials due to changing environmental conditions, both numerical and experimental studies are performed. In order to study the problem numerically, a high-fidelity finite element model (FEM) has been developed (Figure 3). The FEM is based on a simple aluminum plate with two piezoelectric Lead Zirconate Titanate (PZT) disk transducers (diameter: 6.35 mm; thickness: 0.25 mm) attached to the plate through a thin layer of adhesive material (Loctite EA 9394). One transducer acts as the actuator and the other as the sensor in a pitch-catch mode. A 5-peak tone burst signal is applied on the actuator and the corresponding signal is received at the sensor.

Monte Carlo (MC) simulations have been performed to investigate the effect of temperature on a statistical basis. A baseline temperature of 20 ^{0}C was selected to run the MC simulations. Then, a standard deviation of 0.5 ^{0}C was assumed and samples were drawn assuming Gaussian distribution. Thirty simulations were subsequently performed for each base temperature. Next, experiments were performed on a rectangular aluminum plate under ambient temperature (Figure 4). The aluminum plate was outfitted with two piezoelectric sensors attached via the use of adhesive (Loctite EA 9394), similar to the FEM. A digital temperature sensor was also attached to the plate in order to measure the temperature during data acquisition.

In order to address the uncertainty quantification due to variations in material properties considering statistical dependence between the components of random elasticity tensors, a second round of MC simulations has been conducted following the procedure outlined in the theoretical formulation section. By defining the mean values of the bulk and shear moduli and assuming that they follow independent Gamma distributions, the statistically dependent random Young's modulus and Poisson ratio can be obtained. These values are then used in the FEM for the MC analysis.

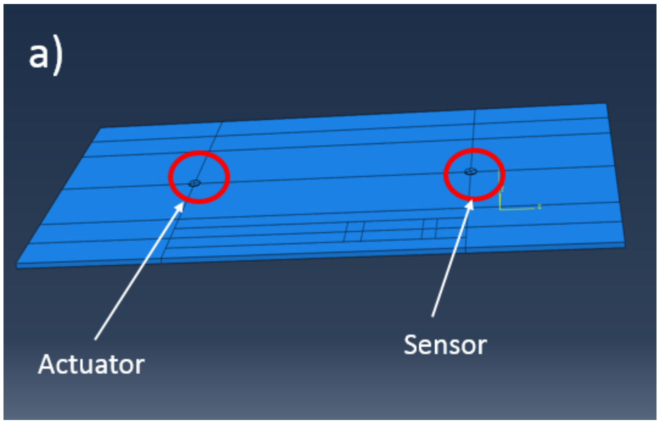

Fig. 3. High fidelity FEM model which consists of an aluminum plate, adhesive and piezo-sensors

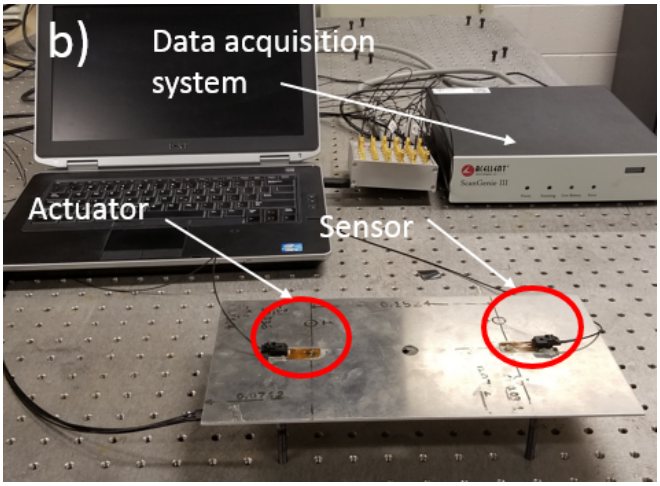

Fig. 4. Experimental setup that corresponds to the FEM simulations

The structure of the paper can be outlined as follows: First, the FEM-based Monte Carlo analysis under varying temperature is presented and the experimental validation of the simulations under varying temperature is addressed. Next, FEM-based Monte Carlo analysis under varying materials properties taking into account the statistical dependence of Young's modulus and Poisson ratio is outlined. Finally, the discussion and critical assessment of the obtained results are presented in terms of the uncertainty involved in active-sensing SHM.

THEORETICAL BACKGROUND

Material properties as random variables

Although in practice materials exhibit random behavior, for theoretical and numerical convenience it is oftentimes assumed that they do preserve deterministic properties. Then it is natural to ask how the components of the elasticity tensors are related. Are these quantities statistically dependent? Physics suggest that the answer to this question might be affirmative. Guilleminot and Soize (Ref. 16) have provided a statistical framework for modeling such dependencies between elasticity tensors by invoking Information Theory and Maximum Entropy Principle. As a result of this analysis, it can be deduced that the Young's modulus and Poisson ratio are not independent, but *statistically dependent Gamma distributed random variables*. A brief overview and derivation is provided in the following (for the detailed formulation the interested reader may refer to (Ref. 17).

Let $\mathbb{E}la$ be the set of all the fourth order elasticity tensors verifying the usual properties of symmetries and positiveness. Hence, $\mathbb{E}la^{sym} \subseteq \mathbb{E}la$ defines the subset of all the fourth order elasticity tensors that belong to the material symmetry class "sym". It is known that any element $[\![C^{sym}]\!] \in \mathbb{E}la^{sym}$ can be decomposed as (Ref. 17):

$$[\![C^{sym}]\!] = \sum_{i=1}^{N} c_i [\![E^{(i)}_{sym}]\!] \tag{1}$$

where $[\![E^{(i)}_{sym}]\!], i = 1, \ldots, N$ is a tensor basis and $c^N_{i=1}$ is a set of coefficients satisfying some algebraic properties related to the positiveness of $[\![C^{sym}]\!]$

Extending the aforementioned decomposition to the case of random elasticity tensors, $[\![C^{sym}]\!]$ then denotes the random variables with values in $\mathbb{E}la^{sym}$, whose probability distribution is sought and can be written as:

$$[\![C^{sym}]\!] = \sum_{i=1}^{N} C_i [\![E^{(i)}_{sym}]\!] \tag{2}$$

where $C^N_{i=1}$ is now a set of random variables whose probability distributions and mutual statistical dependence must be defined.

The values of parameter N is given in Table 1 for the eight linear elastic symmetries. Let the isotropic random elasticity matrix $[C]$ be decomposed as:

$$[C] = 3C_1[E^{(1)}] + 2C_2[E^{(2)}] \tag{3}$$

with C_1 designating the random bulk modulus, C_2 the random shear modulus, E_1 and E_2 being the matrix representation of the classical fourth order symmetric tensors $[\![E^{(1)}]\!]$ and $[\![E^{(2)}]\!]$ defined as:

$$[\![E^{(1)}]\!]_{ijkl} = (1/3)\delta_{ij}\delta_{kl}, \quad [\![E^{(2)}]\!]_{ijkl} = [\![I]\!]_{ijkl} - [\![E^{(1)}]\!]_{ijkl} \tag{4}$$

Here $[\![I]\!]_{ijkl}$ represents the fourth order symmetric identity tensor.

The probability model for random vector $\mathbf{C}$ can be constructed by invoking the Maximum Entropy principle, which allows for explicit determination of probability distributions under a set of constraints defining some available information. Stated differently,the probability density function estimated by this principle is the function which maximizes the uncertainties under some set of constraints. Mathematically, the constraints can be written as:

$$E\{\mathbf{C}\} = \underline{c}, \underline{c} = (c_1, \ldots, c_N) \tag{5}$$

which means the mean value of the tensor C^{sym} is given, and

$$\int_S P_{\mathbf{c}}(\mathbf{c}) d\mathbf{c} = 1 \tag{6}$$

which means the p.d.f $P_{\mathbf{c}}$ satisfies the usual normalization condition, and

$$E\{log(det(\sum_{i=1}^{N} C_i [\![E^{(i)}_{sym}]\!]))\} = \nu_{\mathbf{c}}, |\ \nu_{\mathbf{c}}\ | < +\infty \tag{7}$$

which means the elasticity tensor has a finite second order moment. It can be shown that the p.d.f $P_{\mathbf{c}}(\mathbf{c})$ takes the general form:

$$P_{\mathbf{c}}(\mathbf{c}) = \mathbf{1}_S(C) k_{sol} exp\{- < \lambda_{sol}, g(c) >\} \tag{8}$$

where $\mathbf{c} \mapsto \mathbf{1}_S$ is the characteristic function of S, $k_{sol} = exp\{-\lambda^0_{sol}\}$ is the normalization constant, $\mathbf{c} \mapsto \mathbf{g}(\mathbf{c})$ is the mapping defined on S such that $\mathbf{g}(\mathbf{c}) = (\mathbf{c}, \phi(\mathbf{c}))$, and the mapping $\phi : S \mapsto R$ is given by:

$$\phi(\mathbf{c}) = log(det(\sum_{i=1}^{N} C_i [\![E^{(i)}_{sym}]\!])) \tag{9}$$

Having recognized these constraints, it can be shown that for the isotropic case:

$$\phi(\mathbf{c}) = log 96 c_1 c_2^5 \tag{10}$$

Therefore, it follows that

$$P_{\mathbf{C}}(\mathbf{c}) = P_{C_1}(c_1) P_{C_2}(c_2) \tag{11}$$

with

$$P_{C_1}(c_1) = \mathbf{1}_{\mathbb{R}^+}(c_1) k_1 c_1^{-\lambda} exp\{-\lambda_1 c_1\}, \tag{12}$$

$$P_{C_2}(c_2) = \mathbf{1}_{\mathbb{R}^+}(c_2) k_2 c_2^{-5\lambda} exp\{-\lambda_2 c_2\}, \tag{13}$$

where k_1 and k_2 are positive normalization constants. Thus, the random bulk and shear moduli are Gamma-distributed statistically independent random variables, with parameters $(\alpha_1, \beta_1) = 1 - \lambda, 1/\lambda_1$ and $(\alpha_2, \beta_2) = (1 - 5\lambda, 1/\lambda_2)$.

The normalization constants k_1 and k_2 are found to be $k_1 = \lambda_1^{(1-\lambda)}/\Gamma(1-\lambda)$ and $k_2 = \lambda_2^{(1-5\lambda)}/\Gamma(1-5\lambda)$. It can also be deduced that $\underline{c}_1 = (1-\lambda)/\lambda_1$ and $\underline{c}_2 = (1-5\lambda)/\lambda_2$.

Thus, it can be said that, for isotropic class, the bulk and shear random moduli C_1 and C_2 are independent Gamma distributed random variables, with parameters $(1-\lambda, \underline{c_1}/1-\lambda)$ and $(1-5\lambda, \underline{c_2}/1-5\lambda)$, where $\underline{c_1}$ and $\underline{c_2}$ are given mean values of C_1 and C_2 and $\lambda \in [-\infty, 1/5]$ is a model parameter controlling the level of statistical fluctuation (Ref. 17).

The coefficients of variation of bulk and shear moduli are then given by $1/\sqrt{1-\lambda}$ and $1/\sqrt{1-5\lambda}$, respectively. It can be observed that the two moduli do not exhibit the same level of fluctuations.

Let E and ν be the random Young modulus and Poisson ratio, associated with the isotropic random elasticity tensor, defined as $E = 9C_1C_2/(3C_1 + C_2)$ and $\nu = (3C_1 - 2C_2)/(6C_1 + 2C_2)$.

The joint p.d.f $(e,n) \mapsto P_{E,\nu}(e,n)$ of random variables E and ν can be readily deduced from Eqs. (11), (12) and (13) and is given by:

$$
\begin{aligned}
&P_{E,\nu}(e,n) \\
&= \mathbf{1}_S(e,n)\left(\frac{e}{3(1-2n)}\right)^{-\lambda}\left(\frac{e}{2(1+n)}\right)^{-5\lambda}\frac{e}{2(1+n)^2(1-2n)^2} \\
&\quad \times exp\left\{-\lambda_1\frac{e}{3(1-2n)} - \lambda_2\frac{e}{2(1+n)}\right\}
\end{aligned}
\tag{14}
$$

with $S = [0,+\infty] \times [-1,1/2]$. As a result, the random Young modulus and Poisson ratio turn out to be statistically dependent random variables.

Based on this theoretical formulation, the implementation of the statistical dependency between Young modulus and Poisson ratio can be realized with the following equations:

$$C_1 \equiv \Gamma(\alpha_1,\beta_1), \quad \text{with} \quad \alpha_1 = 1-\lambda_1,\ \beta_1 = \frac{\underline{c}_1}{1-\lambda_1} \tag{15}$$

$$C_2 \equiv \Gamma(\alpha_2,\beta_2), \quad \text{with} \quad \alpha_2 = 1-\lambda_2,\ \beta_2 = \frac{\underline{c}_2}{1-\lambda_2} \tag{16}$$

The mean value of the bulk modulus $\underline{c}_1$ and shear modulus $\underline{c}_2$ can be calculated using the following equations:

$$\underline{c}_1 = \frac{\underline{E}}{3(1-2\underline{\nu})}, \quad \underline{c}_2 = \frac{\underline{E}}{2(1+\underline{\nu})} \tag{17}$$

where $\underline{E}$ is the mean value of Young's modulus and $\underline{\nu}$ represents the mean value of the Poisson ratio.

Now, the Young modulus (E) and Poisson ratio (ν) are related to the bulk modulus (C_1) and shear modulus (C_2) through the following equations:

$$E = \frac{9C_1C_2}{(3C_1+C_2)}, \quad \nu = \frac{(3C_1-2C_2)}{(6C_1+2C_2)} \tag{18}$$

Although the Young modulus and Poisson ratio are statistically dependent Gamma distributed random variables, they can be realized through two independent Gamma distributed random variables, namely, bulk modulus and shear modulus (Ref. 17).

The material density ρ can also be randomized using Gamma distribution around its mean value as follows:

$$\rho \equiv \Gamma(\alpha_3,\beta_3), \quad \text{with} \quad \alpha_3 = 1-\lambda_3,\ \beta_3 = \frac{\underline{\rho}}{1-\lambda_3} \tag{19}$$

where $\lambda_3 \in [-\infty,1]$ controls the statistical fluctuation.

Table 1. Dimension N for all material symmetry classes

Material symmetry	N
Isotropic	2
Cubic	3
Transversely isotropic	5
Trigonal	6
Tetragonal	6 or 7
Orthotropic	9
Monoclinic	13
Triclinic	21

Table 2. Nominal material property values at 25 ^{0}C

Materials	Property name	Values
Piezo-electric: PZT-5A	Density (ρ)	7750 kg/m^3
	Young's modulus (GPa)	$E_{11} = E_{22} = 60.97$ $E_{33} = 53.19$
	Poisson ratio	$\nu_{13} = \nu_{23} = 0.4402$ $\nu_{12} = 0.35$
	Piezo-elctric charge constant (m/V)	$d_{31} = d_{32}$ =171$e-12$ $d_{33} = 374e-12$ $d_{15} = d_{24}$ =558$e-12$
	Dielectric constant	$\varepsilon_{11} = \varepsilon_{22} = 15.32e-9$ $\varepsilon_{33} = 15e-9$
Aluminum	Density (ρ) (Kg/m^3)	2700
	Young's modulus (E GPa)	68.9
	Poisson ratio	0.33
Adhesive	Density (ρ) (Kg/m^3)	1100
	Young's modulus (E GPa)	2.19
	Poisson ratio	0.30

Materials properties as function of temperature

In order to investigate the effect of temperature on the propagation of lamb waves and the associated uncertainty, the materials properties that constitute the SHM system are considered as functions of temperature T. As a result, as the temperature changes, the corresponding material properties also change according to the empirical formulas that are derived experimentally (Refs. 18–20). In this way, it is possible to incorporate the effect of temperature into the numerical simulation approach, and thereby investigate the uncertainty that is initiated by the change in temperature. In this study, the SHM system consists of an aluminum plate, piezo-electric sensors and adhesive materials that bond the piezo-electric sensors with the aluminum plate (Ref. 13). The nominal values of the material properties have been provided in Table 2.

The established functional relationships are outlined in the following.

Properties of piezoelectric materials:

$$\frac{\partial \rho}{\partial T} = 7751.80 - 7.26e-02T$$

$$E_{11} = E_{22} = 60.45 + 2.09e-02T$$

$$E_{33} = 52.95 + 9.8e-03T$$

$$\nu_{13} = \nu_{23} = 0.43 + 3e - 04T - 3e - 06T^2 - 1e - 09T^3$$

$$\nu_{12} = 0.35 + 2e - 04T - 8e - 07T^2 + 2e - 09T^3$$

$$d_{31} = d_{32} = 170.78 - 7.1e - 03T + 6e - 04T^2 + 2e - 16T^3$$

$$d_{33} = 369.12 + 1.49e - 01T + 1.9e - 03T^2 - 4e - 09T^3$$

$$d_{15} = d_{24} = 556 + 4.9e - 02T + 2e - 06T^2 - 2e - 09T^3$$

$$\varepsilon_{11} = \varepsilon_{22}$$
$$= 14.9e - 09 + 1.42e - 11T + 9.74e - 14T^2 + 4.43e - 17T^3$$

$$\varepsilon_{33}$$
$$= 14.60e - 09 + 1.47e - 11T + 1.18e - 13T^2 - 5.31e - 18T^3$$

Properties of aluminum:

$$E_{Al} = 69.62 - 2.63e - 02T$$

$$\frac{\partial \rho}{\partial x} = 2794.60 - 1.84e - 01T$$

$$\nu_{Al} = 0.32 + 3e - 04T$$

Properties of the adhesive:

$$E_{adh} = 3.2 - 0.065T + 1.18e - 03T^2 - 7.72e - 06T^3$$

$$G_{adh} = 1 + 0.001T - 4e - 05T^2$$

WAVE PROPAGATION NUMERICAL SIMULATIONS

In order to simulate the effect of temperature and induced variation in material properties, a high fidelity finite element model was constructed by using commercial finite element software ABAQUS 2018. At the beginning, three separate parts were created namely: an aluminum plate, adhesive, and piezo-electric disk (PZT) following the dimension given in Table 3. Then material properties were defined for each part and assigned to the individual sections. The material properties of aluminum, adhesive and PZT can be found in Table 2. Once the material properties were assigned to the specific sections, all separate parts are assembled together to form a unified part or model. Then, interactions between different parts were created by defining master and slave surfaces. The interaction between the PZT and adhesive were created by selecting the bottom surface of PZT as the master surface and the top surface of adhesive as the slave surface. This has to be done for each pair of adhesive and PZT disk. The discretization method has to be surface to surface.

Then interaction properties were defined, namely, tangential and normal behavior. Under tangential behavior, rough friction formulation was used. Under normal behavior, hard contact was selected for pressure-overclosure option. Then constraints were defined between aluminum and adhesive, as well as PZT and adhesive as much of the same way as interactions were defined. Abaqus implicit or standard were used instead of Abaqus explicit, as Abaqus explicit cannot handle PZT elements.

Table 3. Dimensions of aluminum plate, PZT sensors and adhesive.

Object	Dimension
Thickness of aluminum plate	2.286 mm
Thickness of PZT sensor	0.25 mm
Diameter of PZT sensor	6.35 mm
Thickness of adhesive	0.05 mm
Length of aluminum plate	304.8 mm
Width of aluminum plate	152.4 mm

For the wave propagation simulations, a total time period of 0.0001 s and a time step or incrementation of $1e - 7$ s were used. For defining the actuation signal, a 5-peak-tone burst signal with a center frequency of 250 KHz was used. As boundary conditions, the two ends of the aluminum plate were kept fixed. Then an electric potential boundary condition was applied at two end surfaces of piezo-electric disk. An electric potential of zero volt and 100 volt were applied at the bottom and top surfaces of the piezoelectric actuator disk, respectively. This sets up an electric field between the two surfaces of disk. For the sensor disk, zero voltage is applied only at the bottom surface and top surface is kept free.

The electric potential (EPOT) is selected as the response signal from the piezo-sensor disk. The output signal can be collected from ant single node on the top surface of the PZT sensor. However, signals obtained obtained from different nodes on the surface are different. Hence, it is necessary to obtain the average of all the signals from all the nodes on the top surface of the PZT sensor. This task of averaging can be performed by using equation constraints. Under an equation constraint, a single node is selected as a master node and all other nodes on the surface are constrained with respect to this master node. This forces the electric potential to be same on all other nodes on the surface as same as of the master node. It was found that averaging the signals from all the nodes on the surface is equivalent to using the equation constraint where a master node is used to constrain all other nodes on the surface. The coefficient used for the master node and the other nodes were 1 and -1, respectively. The degrees of freedom used for PZT material were 9.

In order to facilitate meshing, partitioning was performed on all of the three parts, namely, aluminum plate, adhesive materials and PZT disk. For all three parts, structured hexahedron mesh was used. In order to select the mesh size, a convergence study was performed. Based on this study, a global mesh size of 0.001 was chosen for the aluminum plate. The total number of elements in the plate were 93330. For the adhesive and PZT material, a global mesh size of 0.0004 was used. The total number of elements in adhesive and PZT disk were 480. It was ensured that at least 20 elements exist per wave length. The mesh size can be further reduced, but that increases computational cost with no significant increase in the accuracy.

Linear 3D stress element (C3D8R) were selected. For the PZT disk, 8-node linear piezo-electric brick elements were used.

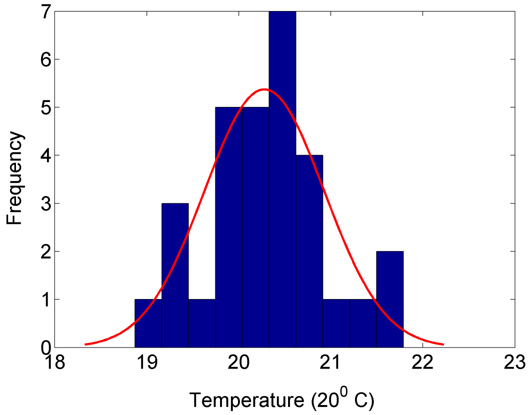

Fig. 5. Temperature distribution with a mean of 20 ^{0}**C.**

With all these specifications, a single simulation takes about 6 hours.

Temperature simulations

In order to investigate and quantify the uncertainty involved in the propagation of Lamb waves due to changes in temperature, the material properties were considered to be a function of temperature according to the equations provided in the theory section. This functional dependence in material properties is reflected in the output signal. It is assumed that temperature follows a normal distribution. For simulation purposes, the mean of the temperature normal distribution was assumed 20 ^{0}C. Then, random samples were drawn from this distribution with a standard deviation of 0.5 ^{0}C. For this study, 30 samples were drawn from the distribution. It has been shown that at least 28 samples are required to properly represent a normal distribution (Ref. 21). For each drawn temperature sample, a separate simulation was conducted by changing 20 material parameters (see equations of previous section) and the output signals were collected. Once all the output signals were collected for the drawn samples, statistical analysis was performed to quantify the uncertainty involved in the wave propagation. Figure 5 shows the distribution of temperature that was used in the simulations.

Material properties simulations

In order to numerically study the effects of variation in material properties on the propagation of Lamb waves, Young's modulus, Poisson ratio, and material density were considered as random variables. From the theoretical formulation, it was deduced that Young's modulus and Poisson ratio are dependent random variables and they jointly follow Gamma distribution. Sixty samples were drawn from this Gamma probability distribution taking into account the dependency between Young's modulus and Poisson ratio. The mean value for Young's modulus was taken to be 68.9 GPa with a standard deviation of 1.332 GPa. The mean value of Poisson ratio was taken to be 0.33 with a standard deviation of 0.007. The value of the parameter λ that controls the statistical fluctuation was selected as -450.

Table 4. Young's modulus variation for aluminum 6061.

	Mean	Standard deviation
Suresh (Ref. 25)	66.4795 GPa	5.0168 GPa
Oliver (Ref. 26)	81.6117 GPa	2.2018 GPa
Doermer (Ref. 27)	81.2671 GPa	2.2188 GPa

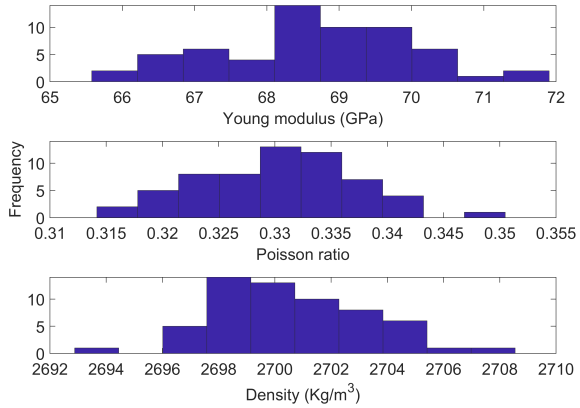

Fig. 6. This plot shows the distribution of material properties used in the simulation

The density of the aluminum plate also follows a Gamma distribution (Ref. 22). The mean value for density was selected as 2700 kg/m^3 with a standard deviation of 2.7022 kg/m^3 (Refs. 23, 24). The value of the parameter λ was chosen to be -800000 in order to achieve the specified standard deviation.

The value of the standard deviation or fluctuation of Young's modulus of the aluminum plate (aluminum 6061) was chosen to be 1.332 GPa which was motivated by experimental studies carried out by several researchers such as (Refs. 25–27). The summary of the findings from these experimental studies are summarized in table 4. The standard deviation of Poisson ratio for an aluminum plate is controlled by the standard deviation of Young's modulus as they are considered dependent random variables.

Once the sample of E, ν, and ρ were drawn from their respective distribution, for each triplet (E, ν, and ρ where E and ν dependent), a separate simulation was performed and output signal was collected. In this way, 60 output signals were recorded and uncertainty involved were quantified. The distribution of materials properties can be seen from figure 6

UNCERTAINTY QUANTIFICATION: RESULTS AND DISCUSSION

Temperature effects

Figure 7 shows the results of 30 simulations for 30 different temperatures, plotted on the same graph, that were drawn from a normal distribution. The signals from the time instant $3e-5$ seconds to $4.5e-5$ seconds constitute the S_0 mode which has 5 distinct peaks and the signals from $5.5e-5$ seconds to $7.5e-5$ seconds constitute the A_0 mode which also

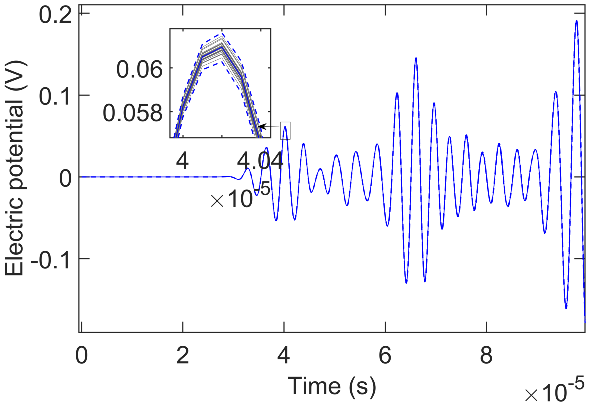

Fig. 7. Uncertainty quantification due to temperature. The dotted line represents the ± 3 standard deviations and the solid line represents the signal mean.

has 5 distinct peaks. However, the third peak of both S_0 and A_0 mode are more pronounced than all other peaks. In this case, the peaks of S_0 mode is smaller than the peaks of A_0 mode. After the time instant $7.5e-5$, the rest of the peaks are considered as coming from the boundary reflections. When all the 30 plots are overlaid on each other, the variation in the signal due to the change in temperature is not apparent. However, in the inset plot which has been zoomed in from the third peak of the S_0 mode does show a marked difference between the signals. The amplitude of the third peak of the of the S_0 mode, which is the most prominent peak in the S_0 mode, is seen to vary between 0.060 and 0.062 V.

In the inset plot, the dotted blue line on the top and bottom represents the ± 3 standard deviations of the signal. The solid line represents the mean of all 30 signals. It can also be observed that the standard deviation near the peak of the signal is much higher than the standard deviation of the signal that is offset from the peak. Another important observation from this inset plot is that the maximum value of the peak occurs at the same time instant, that is, no change in the time of flight (phase) of the wave packet occurs when the standard deviation of the temperature distribution is low. In order to provide a single maximum or minimum value of the signal, a Hilbert transform was performed on the S_0 and A_0 modes of all the signals and their minimum and maximum values were identified. The results are shown in Table 5

Figure 8 shows the error bar representation of the variation of all 30 signals over the entire time period of the output signal. These error bars have been plotted at a specific time interval over the entire signal and represent ± 3 standard deviations of the signal. For example, by zooming in on the second peak of the A_0 mode, it can be deducted that the variation would be confined between 0.1 and 0.105 V for this specific temperature distribution. For real life applications, if the temperature distribution of the environment is specified or determined, then it is possible to predict what would be the uncertainty in the wave propagation and construct the SHM system accordingly so that it would take into account that uncertainty due to temperature.

Table 5. Hilbert transform statistics of the S_0 and A_0 modes due to temperature variation.

	S_0 mode	A_0 mode
Maximum	0.0618 V	0.1464 V
Minimum	0.0609 V	0.1451 V
Mean	0.0613 V	0.1457 V
Standard deviation	$2.088E-4$ V	$2.796E-4$ V

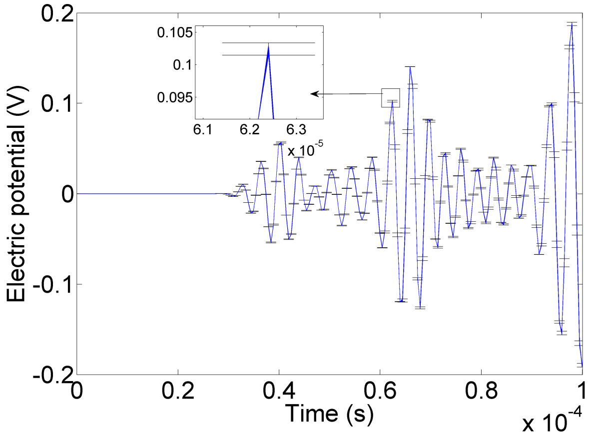

Fig. 8. Uncertainty quantification due to temperature. The error bar represents the ± 3 standard deviation and has been plotted against the whole signal.

In order to investigate the effects of temperature on the propagation of Lamb waves, a wide range of temperatures were considered. For this purpose, 16 simulations were carried out from 20 ^{0}C to 100 ^{0}C with an increment of 5 ^{0}C. In Figure 9, four output signals are plotted simultaneously, which corresponds to 25 ^{0}C, 45 ^{0}C, 65 ^{0}C and 85 ^{0}C. By zooming in on the 3rd peak of the A_0 mode, it can be observed that the max amplitude as well as the phase of each signal changes which is in contrast to Figure 7 where only the maximum amplitude changes.

It can also be observed that the change in amplitude with the increase in temperature is not linear. From 25 ^{0}C to 45 ^{0}C, the amplitude of the signal increases. Then, from 45 ^{0}C to 65 ^{0}C and from 65 ^{0}C to 85 ^{0}C, the amplitude gradually decreases. This nonlinearity in amplitude change may be attributed to the fact that the PZT disks are mounted on the aluminum plate through adhesives which are polymeric materials. At higher temperature, these polymeric materials may soften due to the increased vibration of the polymeric chains. This softening effect may hamper the proper stress transfer between the aluminum plate and PZT sensors which would result in a decreased voltage in the PZT sensor (Ref. 20).

Although the amplitude change is nonlinear, the phase change due to the increase in temperature is linear. As the temperature increases, the material expands and this expansion would delay the wave to reach a certain point. It can be observed from Figure 9 that with the increase in temperature, the peak of each signal shifts to the right.

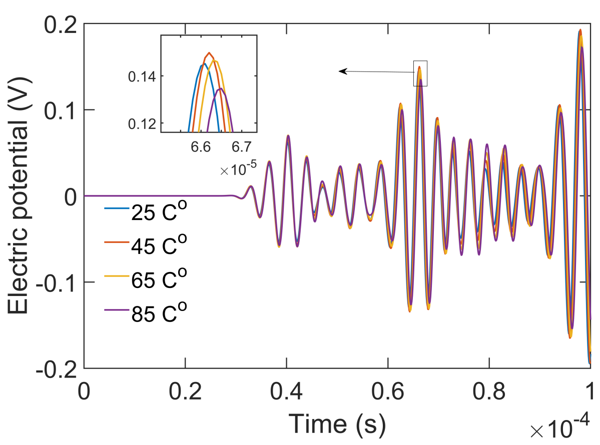

Fig. 9. Wave propagation signals under increasing temperature.

Figure 10 depicts the change in indicative damage indices (DIs) proposed in the literature due to temperature variation. A normalized Root Mean Square Deviation (RMSD) DI can be defined as the ratio of the sum of the scattered signal squared to the sum of the baseline signal squared. Mathematically,

$$DI = \frac{\sum_{n=1}^{N}(V_{inspection}[t] - V_{baseline}[t])^2}{\sum_{n=1}^{N}(V_{baseline}[t])^2} \tag{20}$$

The difference between the inspected signal and the baseline signal is called the scattered signal. Different researchers have proposed different formulations for damage indices which often do not have a theoretical background, but are rather based on signal processing and normalization techniques. However, the sensitivity to the damage provided by a damage index depends on how that damage index has been formulated. In order to study the effect of temperature on the damage index, two different damage indices are presently considered (Refs. 2, 28):

$$DI_{\text{Qui}} = 1 - \sqrt{\frac{\sum_{t=1}^{N}(y_h[t] \cdot y_d[t])^2}{\sum_{t=1}^{N} y_d^2[t] \cdot \sum_{t=1}^{N} y_h^2[t]}} \tag{21}$$

and

$$DI_{\text{Janapati}} = \sum_{t=1}^{N}(N_{damage} - N_{reference})^2 \tag{22}$$

with

$$N_{damage} = \frac{y_d[t]}{\sqrt{\sum_{t=1}^{N} y_d^2[t]}}$$

$$N_{reference} = \frac{\sum_{t=1}^{N}(y_h[t] \cdot N_{damage})}{\sum_{t=1}^{N} y_h^2[t]} \cdot y_h[t]$$

with $y_h[t]$ designating the healthy or baseline signal and $y_d[t]$ the unknown/damaged signal.

In Figure 10, the value of the signal at 20 ^{0}C has been considered as the baseline signal. The value of the signal for all other temperatures may be considered as the unknown (or damaged) signal.

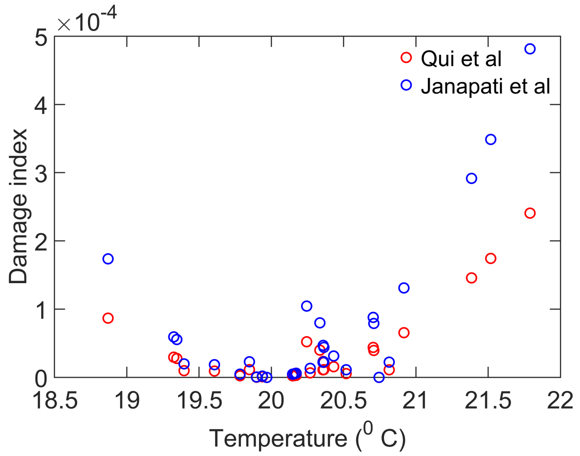

Fig. 10. Damage index variation for a normally distributed temperature variation with a mean of 20 ^{0}C and standard deviation of 0.5 ^{0}C.

In Figure 10, the blue dots corresponds to the damage index provided by Janapati et al. (Ref. 2) while the red dots correspond to the damage index provided by Qui et al. (Ref. 28). It can be observed that for a specific temperature, the damage index provided by Janapati et al. has higher value than that of Qui et al. which suggests that the former one may have a higher sensitivity to damage.

In order to verify this numerical results as well as to gain more insight on the effect of temperature on the wave propagation, a series of experiments were performed both in ambient and elevated temperatures. Figure 11 shows 50 experimental signal plotted on the same graph which have been collected in ambient lab temperature. The third peak of the A_0 mode has been zoomed in at the inset plot. The two dotted lines at the top and bottom represent the ± 3 standard deviations, respectively. The solid line represents the mean of the signal. It can be observed that, although the experiment has been performed at the ambient temperature, the signals occupy most of the region within the ± 3 standard deviation, and even exceed in one case. This variation may be due to the small change in temperature about a mean ambient temperature, similar to the case in Figure 7, which has been studied numerically.

In order to explore this phenomenon more rigorously, a highly sensitive temperature sensor was mounted to the aluminum plate, which can measure slight variations in surrounding temperature. Wave propagation signals were collected for about a month. In each day, at least forty signals were collected at different time instants and the corresponding temperature was also recorded. Figure 12 shows the temperature distribution for 11 representative days. The box plot for each day shows the distribution of 40 recorded temperatures which corresponds to the forty recorded wave signals obtained at different instant of time within a single day.

The horizontal red line in the box plot represents the mean value of the temperature distribution. The blue box represents the inter-quartile range, that is, from 25th to 75th percentile values. The two whiskers on both sides represent the range which is 1.5 times the inter-quartile range. The red dots rep-

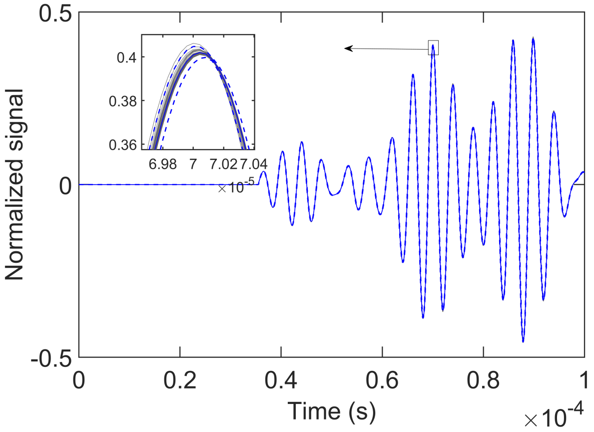

Fig. 11. Experimental signals collected at ambient lab temperature showing variations in their amplitude. In the inset plot, the solid line represents the mean and dotted lines represent the ± 3 standard deviation.

resent the individual outliers or the values that falls outside the 1.5 times the inter-quartile range.

From Figure 12, it can be observed that a potential seasonal variation exists between the mean temperatures of all the days which fluctuate about 24 ^{0}C. The temperature distribution of day 3 is slightly off from the usual trend. In order to confirm such a seasonal trend, data obtained during a longer period of time would be required to confirm this observation.

Having known this temperature distribution for all eleven days from Figure 12, the associated uncertainty in wave propagation on an aluminum plate is quantified by finding the percentage change of the amplitude of the S_0 and A_0 modes for each individual day. The results are presented in Figure 13 and Figure 14 for the S_0 and A_0 modes, respectively. For each day, forty signals were used in the analysis.

A closer observation of Figure 13 reveals that a potential seasonal trend exists between the mean values of the S_0 amplitude change over the eleven days. The same seasonal trend can also be found in Figure 14 for A_0 amplitude change. In Figures 13 and 14, normalization was performed with respect to the maximum value of the S_0 and A_0 mode amplitude. From Figure 13, it can be readily observed that the percentage amplitude change for S_0 mode ranges within 1-1.5% for all days. On the other hand, from Figure 14, it can be observed that the percentage amplitude change for A_0 mode ranges between 0.3-0.6% for all days. Although the absolute value of amplitude variation is higher for the A_0 mode than in S_0 mode, the percentage variation in amplitude change is higher for the S_0 mode. Therefore, it can be concluded that the uncertainty involved in the variation of amplitude due to the temperature change is higher in S_0 mode and SHM systems should be designed taking into account this uncertainty.

Figure 15 shows the normalized mean amplitude of S_0 and A_0 modes and associated standard deviation as a function of the wave actuation center frequency for a single day. The center frequency of the input signal was varied from 250 KHz to 700 KHz and corresponding output signals were recorded.

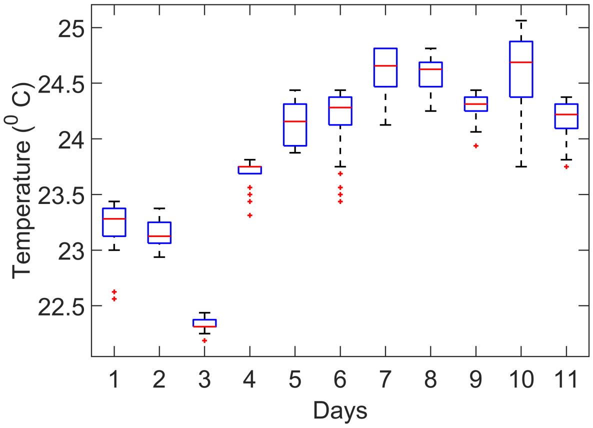

Fig. 12. Temperature distribution for eleven different days. Each day contains 40 temperature recordings. The red line in the boxplot represents the mean and the blue box represents the inter-quartile range.

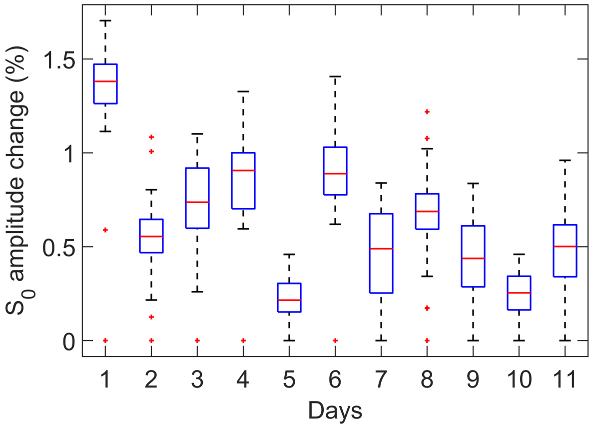

Fig. 13. Amplitude change percentage of the S_0 mode over the eleven days. The red line in the boxplot represents the mean and the blue box represents the inter-quartile range.

For each frequency, 40 signals were collected and their mean and standard deviation were determined. From Figure 15, it can be observed that as the frequency increases from 250 to 500 KHz, the amplitude of S_0 mode gradually increases and becomes maximum at 500 KHz. From 550 KHz the frequency of the S_0 mode starts to decrease again, however, the amount of decrease is very small. For the A_0 mode, the frequency gradually decreases from 250 to 350 KHz, and then increases again until 550 KHz. After that, it starts to decrease again. The amplitude of A_0 mode becomes maximum at 550 KHz.

Material properties analysis

Figure 16 shows the plot of 60 different signals which were generated taking into account the variation in material properties. The solid blue line represents the mean of all 60 signals and the dotted blue lines on top and bottom represent the ± 3 standard deviation of the signals. It can be observed that due to the change in material properties, the amplitude of the signals were affected as well as their phase.

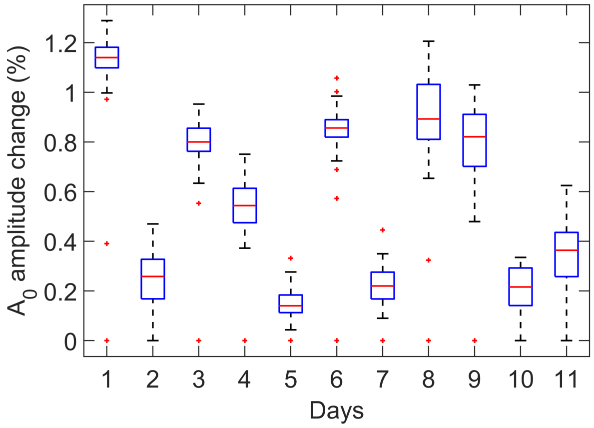

Fig. 14. Amplitude change percentage of the A_0 mode over the eleven days. The red line in the boxplot represents the mean and the blue box represents the inter-quartile range.

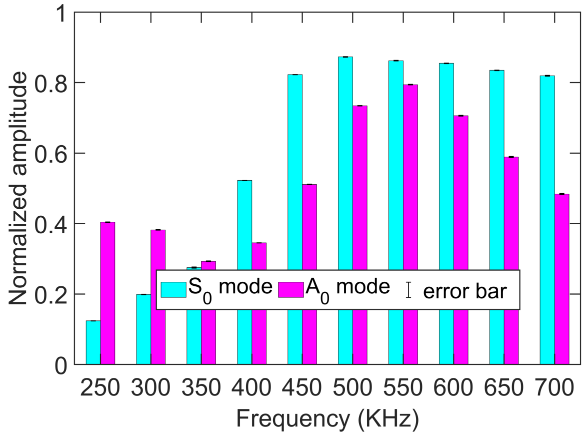

Fig. 15. Amplitude variation of S_0 and A_0 modes for different actuation frequencies for a single day.

A Hilbert transform was also performed for the S_0 and A_0 modes, and their minimum and maximum values were determined. Table 6 shows the mean, standard deviation, minimum and maximum values of the Hilbert transform due to the variation in material properties. In this case, Young's modulus and Poisson ratio were considered as random variables of dependent Gamma distributions and they were sampled from their joint probability distribution. Density was also considered as a Gamma distributed random variable.

As the variation in material properties causes changes in the signal amplitude and phase, it can mask the effect of damage.

Table 6. Hilbert transform statistics of the S_0 and A_0 modes due to variation in material properties.

	S_0 mode	A_0 mode
Maximum	0.0413 V	0.0992 V
Minimum	0.0356 V	0.0774 V
Mean	0.0383 V	0.0881 V
Standard deviation	0.0012 V	0.0052 V

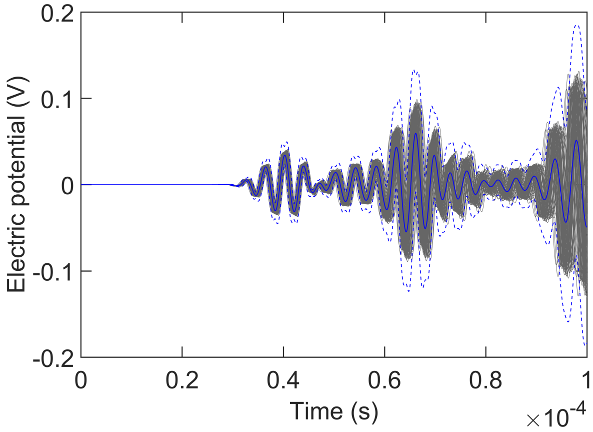

Fig. 16. Variation in the propagation of the waves due to variation in material properties.

Hence, it is of interest to investigate the damage index variation due to variation in material properties. Unlike the damage index due to the variation in temperature, two variables are involved in this case, namely, the Young's modulus and Poisson ratio, as they are dependent on each other and they jointly contribute to the damage index. Figure 17, depicts the change in the damage index due to the joint change in Young's modulus and Poisson ratio. Here, Young's modulus has been plotted in the x-axis and Poisson ratio has been plotted in the y-axis, while the corresponding damage index has been plotted in the z-axis (MATLAB function *scatter3.m*). For calculating the damage index, two different DI formulations were used (Refs. 2, 28). The blue dots indicate the damage index provided by Janapati et al. while the red dots indicate the damage index provided by Qui et al. It can be observed from Figure 17 that the damage index index provided by Janapati et al. is higher than that of Qui et al. for the same material properties, that is, the Janapati DI is more sensitive to the variation in material properties.

The baseline signal was constructed by considering the nominal values of the material properties for aluminum plate, i.e. 68.9 GPa and 0.33 were the nominal values for the Young's modulus and Poisson ratio, respectively. It can be seen from Figure 17 that as the material properties deviate from the nominal values, the calculated DIs increase. Figure 18 depicts the damage index plot for the variation in Young's modulus and density. As the values of Young's modulus and density deviate from the nominal values, the calculated DIs also increase.

CONCLUSIONS

In this study, a preliminary investigation on the variability of the wave propagation due to the variations in temperature as well as material properties was presented. In order to do so, a high fidelity FEM model was constructed and Monte Carlo simulations were performed both for temperature and material properties. For the temperature analysis, samples were drawn from a normal distribution, while for the case of the material properties a thorough theoretical analysis and derivation was

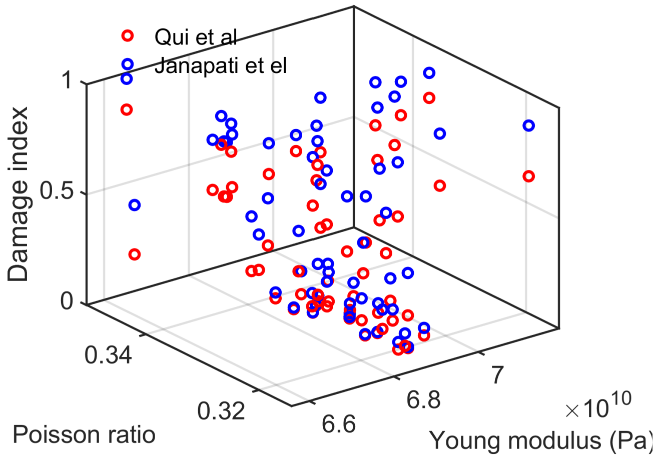

Fig. 17. Variation in the damage index due to the variation in Young's modulus and Poisson ratio based on two different damage index formulations. The Young's modulus and Poisson ratio are considered as dependent random variable.

outlined. Samples were drawn from a Gamma distribution considering the dependency of Young's modulus and Poisson ratio. The variation in the wave propagation signals was quantified based on both numerical simulations and a series of laboratory experiments under both ambient and elevated temperatures. The variation in current state-of-the-art damage index formulations due to temperature as well as material properties was also quantified and assessed. This work constitutes an introductory study aiming to tackle the significant challenge of active-sensing SHM reliability quantification in terms of environmental and material factors. The preliminary results presented herein will pave the way for the postulation of a thorough quantification framework that accounts for environmental and operational variations and uncertainty with the ultimate aim of integrating this analysis with active-sensing SHM technologies in order to increase their robustness and subsequent reliability.

ACKNOWLEDGMENTS

This work is carried out at the Rensselaer Polytechnic Institute under the Army/Navy/NASA Vertical Lift Research Center of Excellence (VLRCOE) Program, grant number W911W61120012, with Dr. Mahendra Bhagwat and Dr. William Lewis as Technical Monitors.

REFERENCES

[1] Doebling, S. W., Farrar, C. R., Prime, M. B., *et al.*, "A summary review of vibration-based damage identification methods," *Shock and vibration digest*, Vol. 30, (2), 1998, pp. 91–105.

[2] Janapati, V., Kopsaftopoulos, F., Li, F., Lee, S., and Chang, F.-K., "Damage detection sensitivity characterization of acousto-ultrasound-based structural health monitoring techniques," *Structural Health Monitoring*, Vol. 15, (2), 2016, pp. 143–161.

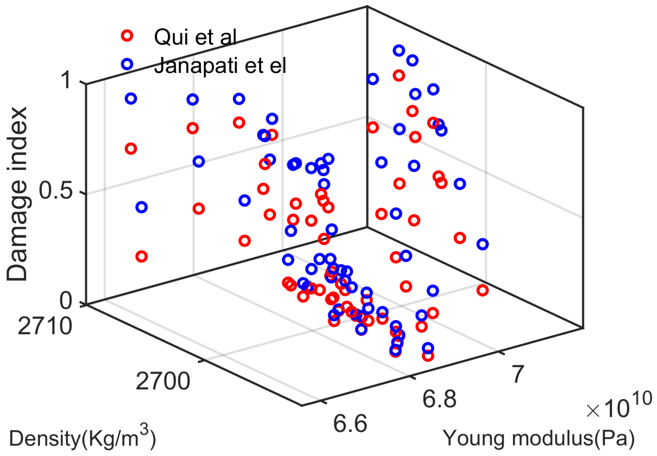

Fig. 18. Variation in the damage index due to the variation in Young's modulus and density based on two different damage index formulations.

[3] Ihn, J. and Chang, F.-K., "Pitch-catch active sensing methods in structural health monitoring for aircraft structures," *Structural Health Monitoring*, Vol. 7, (1), 2008, pp. 5–19.

[4] Kopsaftopoulos, F. P., *Advanced Functional and Sequential Statistical Time Series Methods for Damage Diagnosis in Mechanical Structures*, Ph.D. thesis, Department of Mechanical Engineering & Aeronautics, University of Patras, Patras, Greece, January 2012.

[5] Soize, C., *Uncertainty Quantification*, Springer, 2017.

[6] Worlton, D., "Experimental confirmation of Lamb waves at megacycle frequencies," *Journal of Applied Physics*, Vol. 32, (6), 1961, pp. 967–971.

[7] Konstantinidis, G., Drinkwater, B., and Wilcox, P., "The temperature stability of guided wave structural health monitoring systems," *Smart Materials and Structures*, Vol. 15, (4), 2006, pp. 967.

[8] Croxford, A. J., Wilcox, P. D., Lu, Y., Michaels, J., and Drinkwater, B. W., "Quantification of environmental compensation strategies for guided wave structural health monitoring," Health Monitoring of Structural and Biological Systems 2008, Vol. 6935, 2008.

[9] Vitola, J., Pozo, F., Tibaduiza, D., and Anaya, M., "Distributed piezoelectric sensor system for damage identification in structures subjected to temperature changes," *Sensors*, Vol. 17, (6), 2017, pp. 1252.

[10] Lu, Y. and Michaels, J. E., "A methodology for structural health monitoring with diffuse ultrasonic waves in the presence of temperature variations," *Ultrasonics*, Vol. 43, (9), 2005, pp. 717–731.

[11] Sohn, H., “Effects of environmental and operational variability on structural health monitoring,” *Philosophical Transactions of the Royal Society A: Mathematical, Physical and Engineering Sciences*, Vol. 365, (1851), 2006, pp. 539–560.

[12] Moorty, S. and Roeder, C. W., “Temperature-dependent bridge movements,” *Journal of Structural Engineering*, Vol. 118, (4), 1992, pp. 1090–1105.

[13] Roy, S., Lonkar, K., Janapati, V., and Chang, F.-K., “A novel physics-based temperature compensation model for structural health monitoring using ultrasonic guided waves,” *Structural Health Monitoring*, Vol. 13, (3), 2014, pp. 321–342.

[14] Croxford, A. J., Moll, J., Wilcox, P. D., and Michaels, J. E., “Efficient temperature compensation strategies for guided wave structural health monitoring,” *Ultrasonics*, Vol. 50, (4-5), 2010, pp. 517–528.

[15] Raghavan, A. and Cesnik, C. E., “Effects of elevated temperature on guided-wave structural health monitoring,” *Journal of Intelligent Material Systems and Structures*, Vol. 19, (12), 2008, pp. 1383–1398.

[16] Guilleminot, J. and Soize, C., “On the statistical dependence for the components of random elasticity tensors exhibiting material symmetry properties,” *Journal of elasticity*, Vol. 111, (2), 2013, pp. 109–130.

[17] Guilleminot, J. and Soize, C., “Generalized stochastic approach for constitutive equation in linear elasticity: a random matrix model,” *International Journal for Numerical Methods in Engineering*, Vol. 90, (5), 2012, pp. 613–635.

[18] Brammer, J. and Percival, C., “Elevated-temperature elastic moduli of 2024 aluminum obtained by a laser-pulse technique,” *Experimental Mechanics*, Vol. 10, (6), 1970, pp. 245–250.

[19] Sherrit, S., Yang, G., Wiederick, H., and Mukherjee, B., “Temperature dependence of the dielectric, elastic and piezoelectric material constants of lead zirconate titanate ceramics,” Proceedings of the international conference on smart materials, structures and systems, 1999.

[20] Ha, S., Lonkar, K., Mittal, A., and Chang, F.-K., “Adhesive layer effects on PZT-induced lamb waves at elevated temperatures,” *Structural Health Monitoring*, Vol. 9, (3), 2010, pp. 247–256.

[21] Sugden, R., Smith, T., and Jones, R., “Cochran’s rule for simple random sampling,” *Journal of the Royal Statistical Society: Series B (Statistical Methodology)*, Vol. 62, (4), 2000, pp. 787–793.

[22] Farhat, C., Bos, A., Avery, P., and Soize, C., “Modeling and quantification of model-form uncertainties in eigenvalue computations using a stochastic reduced model,” *AIAA Journal*, Vol. 56, (3), 2017, pp. 1198–1210.

[23] Association, A. *et al.*, *Aluminum: properties and physical metallurgy*, ASM International, 1984.

[24] Mondolfo, L. F., *Aluminum alloys: structure and properties*, Elsevier, 2013.

[25] Dao, M., Chollacoop, N. v., Van Vliet, K., Venkatesh, T., and Suresh, S., “Computational modeling of the forward and reverse problems in instrumented sharp indentation,” *Acta materialia*, Vol. 49, (19), 2001, pp. 3899–3918.

[26] Oliver, W. C. and Pharr, G. M., “An improved technique for determining hardness and elastic modulus using load and displacement sensing indentation experiments,” *Journal of materials research*, Vol. 7, (6), 1992, pp. 1564–1583.

[27] Doerner, M., Gardner, D., and Nix, W., “Plastic properties of thin films on substrates as measured by submicron indentation hardness and substrate curvature techniques,” *Journal of Materials Research*, Vol. 1, (6), 1986, pp. 845–851.

[28] Qiu, L., Yuan, S., Bao, Q., Mei, H., and Ren, Y., “Crack propagation monitoring in a full-scale aircraft fatigue test based on guided wave Gaussian mixture model,” *Smart Materials and Structures*, Vol. 25, 2016, pp. 055048.